# Effects of pivot point and spacing on the aerodynamic characteristics of tilting biplane airfoils

**Ruixue Guo**
Changchun Institute of Optics, Fine Mechanics and Physics
**Xinbiao Pei**
Changchun Institute of Optics, Fine Mechanics and Physics
**Zheng Qiao**
Changchun Institute of Optics, Fine Mechanics and Physics
**Yue Bai** ( baiy@ciomp.ac.cn )
Changchun Institute of Optics, Fine Mechanics and Physics

**Research Article**

**Keywords:** Pivot point, Spacing ratio, Aerodynamic characteristics, Biplane airfoils, Effective angle of attack

**Posted Date:** May 31st, 2022

**DOI:** https://doi.org/10.21203/rs.3.rs-1664694/v1

**Noname manuscript No.**
(will be inserted by the editor)

# Effects of pivot point and spacing on the aerodynamic characteristics of tilting biplane airfoils

**Ruixue Guo · Xinbiao Pei · Zheng Qiao · Yue Bai**

Received: 17 May 2022 / Accepted: date

**Abstract** The effects of pivot locations ($x_p/c$) and spacing ($d_s = \lambda c$) between the biplane airfoils was studied using the numerical method. SST $k-\omega$ turbulence model and U-RANS equations were solved when adopting overset grids. The findings revealed the aerodynamic characteristics of tilting biplane airfoil existed phase lag under five fixed pivot points from leading edge to trailing edge but if the wall effect in the gap was so strong, the hysteresis of $C_{L,lower}$ significantly collapse. Besides, $C_M$ curves drop as pivot moves upward comparing to coincident relative and increasing $\lambda$ could improve total lift coefficients. These results could be explained from the view of vorticity evolution where LEV, SV and TEV showed diverse structures to induce dynamic stall. Additionally, with rearward movement of the pivot point, the emergence of identical flow structures was delayed, and thus aerodynamic characteristics had the high similarity under different $x_p/c$ and $\lambda$. Therefore, a concept of effective angle of attack of biplane airfoils was first proposed and its function introduced a new factor $\lambda$ in order to study the backward shift of pivot point in the centerline.

**Keywords** Pivot point · Spacing ratio · Aerodynamic characteristics · Biplane airfoils · Effective angle of attack

Ruixue Guo
R&D Center of Fine Instruments and Equipment, Changchun Institute of Optics, Fine Mechanics and Physics, Chinese Academy of Sciences, Changchun, 130033;
University of Chinese Academy of Sciences, Beijign, 100049
E-mail: guoruixuefriendly@163.com

Yue Bai (✉)
R&D Center of Fine Instruments and Equipment, Changchun Institute of Optics, Fine Mechanics and Physics, Chinese Academy of Sciences, Changchun, 130033
E-mail: baiy@ciomp.ac.cn

**Nomenclature**

| | |
|---|---|
| $\alpha$ | Angle of attck (°) |
| $\alpha_{stall}$ | Stall angle of attck (°) |
| $\alpha_{geo}$ | Geometric angle of attck (°) |
| $\alpha^*_{eff}$ | Additional angle of attck (°) |
| $\alpha_{eff}$ | Effective angle of attck (°) |
| $\beta_u$, $\beta_l$ | Local position angles of attck (°) |
| $\lambda$ | Spacing ratio between biplane airfoils |
| $c$ | Chord length ($m$) |
| $d_s$ | Vertical distance between biplane airfoils ($m$) |
| $x_p$ | Position of the pivot point ($m$) |
| $\Delta t$ | Time step ($s$) |
| $C_L$ | Instantaneous lift coefficient |
| $C_M$ | Instantaneous moment coefficient |
| $C_{L,lower}$ | Lift coefficient of the lower airfoil |
| $C_{L,upper}$ | Lift coefficient of the upper airfoil |
| $Re$ | Reynolds number ($Re = \rho U_\infty c/\mu$) |
| $U_\infty$ | Freestream velocity ($m/s$) |
| $NACA$ | National Advisory Committee for Aeronautics |
| $MAV$ | Micro aerial vehicle |
| $LE$ | Leading edge |
| $TE$ | Trailing edge |
| $LEV$ | Leading-edge vortex |
| $TEV$ | Tailing-edge vortex |
| $SV$ | Secondary vortex |
| $\downarrow$ | First Tilting Transition (FTT) |
| $\uparrow\uparrow$ | Second Tilting Transition (STT) |

## 1 Introduction

The tilting can be well regarded as a complete stroke of pitching motion. As far as two transition modes of Biplane MAV flight are concerned in Fig. 1(a), the first tilting transition (FTT) occurs from vertical takeoff to cruise, which corresponds to the downstroke of pitching, and the second tilting transition (STT) is operated before vertical landing, just as upstroke. Prominent tilting transition motion takes place with difficulty under the pull of rotors as shown in Fig. 1(b), which has caused great concern in the scholar community for it flies at high angle of attack. This is driven not only by interest in unsteady aerodynamic characteristics of synchronous tilting airfoils but also by the curiosity about the optimal design of biplane configuration.

As is known to all, there are abundant flow phenomena in the pitching case, such as special vortices structures after dynamic stall. Many factors have significant influences over how vortical evolution affects aerodynamic loads. In

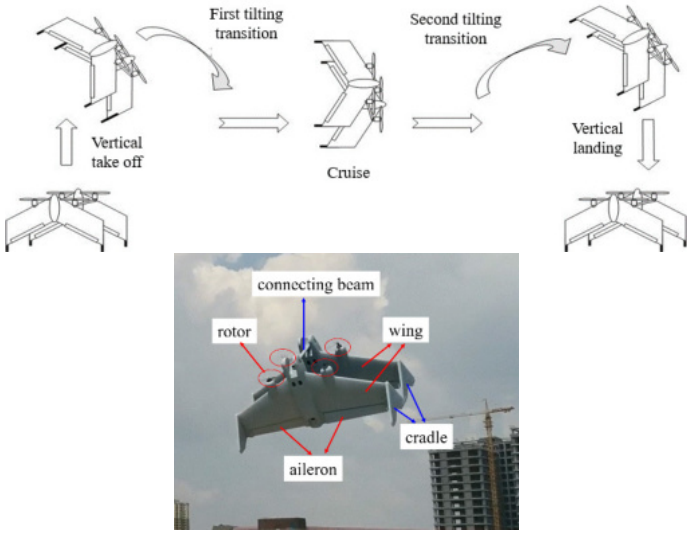


**Fig. 1** (a) Schematic of flight process, (b) tilting transition mode of Biplane MAV.

general, pitching motion of an airfoil or flat plate is dominated by the amplitude $\alpha_m$ [1-3] and reduced frequency $k$ ($k = \pi fc/U_\infty$) [1,2]. Besides, Reynolds number $Re$ [4-7] , turbulence intensity $Tu$ [6], wall effect [8,9] and flexible deformation [10] are noteworthy parameters. Mackowski and Williamson [11] measured the thrust of an airfoil undergoing pure pitching directly, finding that fluid force is largely insensitive to most wake vortex arrangements. Goyaniuk et al. [12] changed the heave stiffness in pitch covering a range of frequency ratios $0.68 < \omega < 1.43$ to deepen the understanding of physical nature of stall flutter. When low-frequency oscillation [13,14], separation point showed quasi-period movement thus flow structures around the airfoil can generate reverse flow region. Additionally, high amplitudes of the pitching motion were also associated with an increased hysteresis of the force coefficients between the upstroke and downstroke [3]. And the onset of vortex formation was found to occur at earlier times with higher amplitude [15].

For biplane or tandem airfoils, the positional relationship of two neighboring airfoils is often the key to the issue that the aerodynamic performances differ from those of a single airfoil. For example, stagger and gap [16,17] in the two-airfoil arrangement have significant influences on each airfoil because of the latter locates at the wake of the former. Direct measurements for the aerodynamic characteristics of two-wing configurations were acquired by Jones et al. [118] for a range of values of stagger and gap. Lagopoulos et al. [19] provided the first explanation for the significant impact of the downstream field to the front foil through change of foil spacing as well as Strouhal number and phasing of tandem flapping foils. In fact, various parameters should be paid more attention. Mean angles of attack [20], Reynolds number [21], flexible extent [22,23] and flapping modes[24-27] have been extensively studied to reveal

the interference effects. Zhou et al. [28] discussed the effects of the position of the mass center on the system's aeroelastic stability.

As mass center, the pivot location is also worthy considering because it affects the flow separation and wake and then plays an important role in the unsteady response of the pitching airfoil. Granlund et al. [29] compared four pivot axis locations of pitching flat plates and proposed the trends of LEV development as the pivot point gradually moved to the trailing edge. Mackowski and Williamson [30] experimentally investigated the propulsive characteristics at $x_p/c$=-1, 0, 0.25, 0.42, 1 and 2 then concluded that the airfoil system with its center of mass fixed at the centroid produced maximum thrust. Yu et al. [31] suggested lift coefficient overall increase with the absolute distance between the pivot point location and the 3/4-chord location. And Li et al. [32] summarized the similarity of aerodynamic load and vortical structures for fixed-pivot pitching airfoils with different pivot locations. Actually, the evolution of the unsteady vortex structures in the wake of the pitching airfoils always could be used to explain the detail of resultant force changes [33,34].

Furthermore, when an oscillating airfoil pitches in a sinusoidal pattern, the turbulent flow separations and reattachments around it induces deep dynamic stalls[35]. The TEVs formed previously now become more compact and it should be noted that the magnitude of the vorticity of the rolling-up vortex is significant [36]. Karbasian and Kim [37] revealed that despite the existence of coherent structures, the interaction of organized vortices is responsible for the complexity of the flow in stall. What's more, Rahman and Tafti [38] gave a more direct explanation that LEVs were responsible for the production of thrust whereas TEVs led to drag. Zhou et al. [39] paid more attention to the boundary layer characteristics near TE. Other nonlinear dynamics [40,41] have also been proved to be related to the generation and evolution of vortices even at transonic flight [42].

Nevertheless, studies on vortex growth, biplane configuration and pivot location effects are insufficient, especially for tilting motion. In order to further explore the above three aspects, a numerical investigation was conducted to analyze the influences of the pivot location with different spacing between biplane airfoils undergoing sinusoidal pitching, which could roughly simulate FTT and STT. We attempted to explain it from the view of the evolution of vortices and proposed the effective angle of attack for biplane configuration.

The writing structure is arranged as follows: methodology and validation were described in Section 2. Then taking $\lambda = 1$ as an example, lift and moment coefficients curves were plotted to describe differences about fixed-pivot ($x_p/c$=0, 0.5, and 1) in the $y^{'}$ direction in Section 3.1; Next, lift coefficient hysteresis loops of biplane airfoils were taken consideration of five cases of fixed-pivot ($x_p/c$=0, 0.25, 0.5, 0.75, and 1) in the chord ($x^{'}$) direction and three spacing ratios ($\lambda$=0.25, 0.5, and 1) were explained in Section 3.2; After that we explored LEV and TEV growth trends at the same angle of attack during FFT and STT in Section 3.3; And we gave the derivation process of the effective angle of attack then verified its feasibility in Section 3.4. At last, in Section 4 we put forward the conclusions in terms of the numerical simulations.

## 2 Numerical Method and Validation

The commercial computational fluid dynamics code ANSYS Fluent 2021 R1 is employed in the present paper. There are following three main aspects: computational domain and grid generation, numerical method, as well as grid and time sensitivity verification.

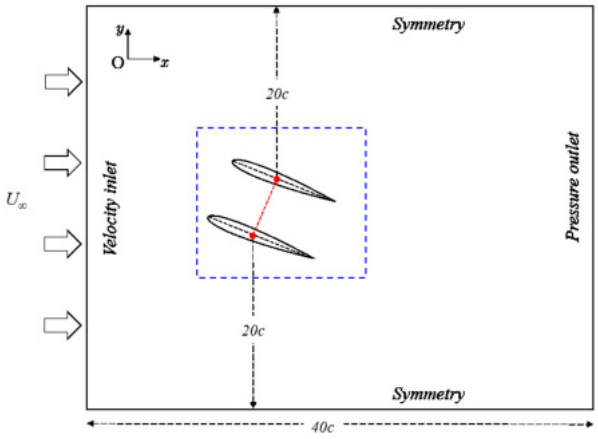


**Fig. 2** Schematic of biplane airfoils and the computational domain.

### 2.1 The computational domain and grid generation

The computational domain with 2D biplane airfoils is abstracted and simplified as represented in Fig. 2. The vertical distances from midpoints of airfoil chord lines to symmetry boundaries remain $20c$. It is seen that the distance from the velocity inlet or pressure outlet to model is defined as $20c$ and $40c$, respectively. Two airfoils (no-slip wall) are taken for calculation, whose identical chord lengths ($c$) equal to $0.15m$. Freestream velocity $U_\infty$ is $14m/s$ and other details will be described in the following sections.

Overset grid technique can provide high quality mesh for airfoil tilting motion. Importantly, $y^+$ value of the first grid near the wall surface is smaller than 1. As Figure 3 shows, background and airfoil grids with refined grids of LE and TE are composed of quadrilateral elements. According to the experiment [43], the pitching angles of attack show a sinusoidal function in the form

$$\alpha(t) = \alpha_0 + \alpha_m \sin(2\pi f t) \tag{1}$$

Here, the reduced frequency $k = \pi f c/U_\infty = 0.1$ and $\alpha_0 = 10^\circ$ with high amplitude $\alpha_m = 15^\circ$. In Fig. 3(c), pivot point is located on centerline and two subdomains pitch with the same angular velocity.

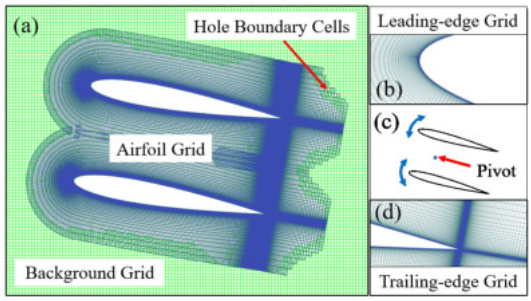


**Fig. 3** Schematic of overset grids: (a) background and airfoil grids, (b) refined leading-edge grid, (c) pitching motion for biplane airfoils, (d) refined trailing-edge grid.

## 2.2 Numerical methods

The 2D U-RANS equations are solved based on the SST $k-\omega$ turbulence model, which is verified the accuracy of predicting flow separations. These equations can be written as:

$$\nabla \cdot \mathbf{u} = 0 \tag{2}$$

$$\frac{\partial \mathbf{u}}{\partial t} + \mathbf{u} \cdot \nabla \mathbf{u} = -\frac{1}{\rho}\nabla p + \nu \nabla^2 \mathbf{u} \tag{3}$$

where $\mathbf{u}$ denotes velocity field; $t$ is the time; $p$ is static pressure; the dimensionless velocity vector and pressure are encapsulated in $\mathbf{q}(x, y, z) = (\mathbf{u}, p)^{\mathrm{T}} = (u, v, p)^{\mathrm{T}}$.

The Coupled algorithm is utilized for pressure-velocity coupling. The momentum and modified turbulent viscosity are second-order upwind scheme, and temporal discretization is performed using a first-order implicit formulation. Besides, the convergence criterion of the iterative calculation is set to $10^{-6}$.

## 2.3 2.3 Grid and time sensitivity verification

In this paper, the independence of the simulations that calculate the lift coefficient ($C_L$) of a pitching airfoil whose pivot is quarter chord point with respect to both spatial and temporal discretization are shown in Fig. 4, respectively. Three sets of grids have been designed: coarse, medium and fine with 14840, 30000 and 100000 cells around the airfoil in corresponding background domain with 40000, 81225 and 240100 cells. Meanwhile, three timesteps are considered: $0.0002s$, $0.0001s$ and $0.00005s$. Obviously, $C_L$ in a whole cycle has a tiny discrepancy between dashed line and chain line. Considering calculation accuracy and cost, the medium grid and $\Delta t = 0.0001s$ are preferred.

Fig. 5 exhibits that comparison of the present numerical results (medium condition) with the experimental result [43] and other numerical simulations

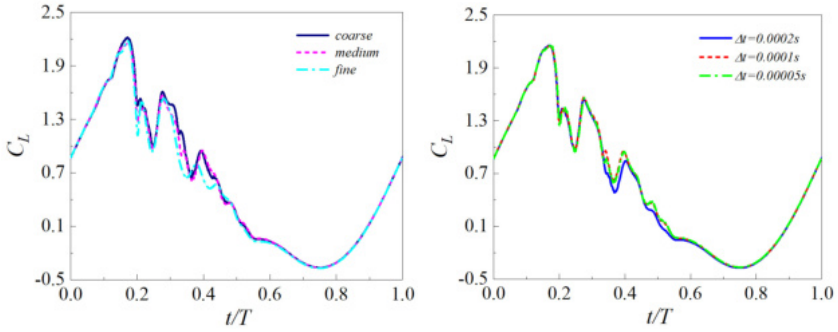


**Fig. 4** Sensitivity of (a) grids, (b) time for a pitching airfoil.

[32,44]. It must be kept in mind that severe flow separation is induced accompanying with complicated flow structures at high angle of attack, which can lead to inaccuracy. From the experimental point of view, another inaccurate factor is the difficulty of measuring the exact pressure because of shedding vortices. Hence, the calculations in all cases are believed the reliability and accuracy with overset grids.

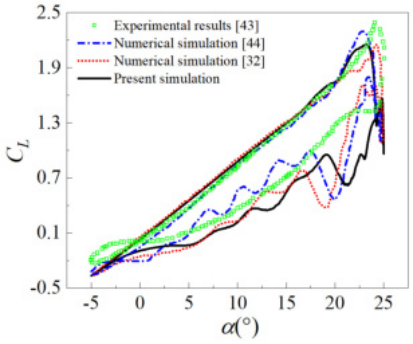


**Fig. 5** Comparison of present numerical results with experimental results and other numerical simulations.

Next, Fig. 6 plots curves of $C_L$ about biplane airfoils for different grids and timesteps. For instance, two airfoil grids with small spacing overlap severely as shown in Fig. 2, logically, this situation should have larger errors. In fact, in FTT especially at the post-stall, the curves for the medium and fine conditions remain marginal differences because of complicated flow interference between two airfoils, whereas coarse condition has worse error. However, $C_{L,lower}$ and $C_{L,upper}$ and the stall moment obtained about $t/T = 0.2$ from the three grids for STT are basically same, as well as the three timesteps. In a word, it is suitable for the medium grid with 81225 background cells and 30000 airfoil cells and $\Delta t = 0.0001s$ to be adopted in the subsequent biplane simulations considering the consumption of computing resources.

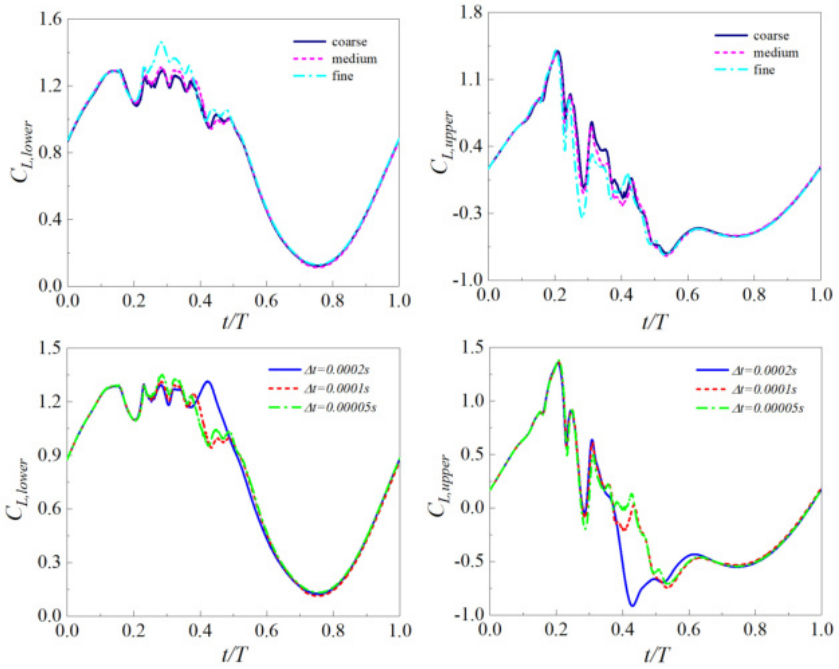


**Fig. 6** (a) Grid sensitivity of the lower airfoil, (b) grid sensitivity of the upper airfoil, (c) time sensitivity of the lower airfoil, (d) time sensitivity of the upper airfoil.

## 3 Results and Discussion

In this section, the aerodynamic characteristics of biplane airfoils undergoing tilting motion are studied for different pivot locations and spacing ratios. Subsequently, we analyzed the vorticity structures to explain the mechanics of flow evolution. A derivation process of effective angles of attack covering two parameters $t$ and $\lambda$ was shown.

### 3.1 Effect of pivot locating in $x^{'}$ and $y^{'}$ directions

Biplane configuration in Fig. 2 contains two NACA0012 airfoils named the lower airfoil and the upper airfoil and the vertical distance between them is defined as $d_s = \lambda c$ where $\lambda$ presents the dimensionless spacing ratio. Additionally, $x$ direction dictates the direction of freestream velocity whereas in coordinate system $x^{'}Oy^{'}$, $x^{'}$ direction represents the direction of chord and $y^{'}$ direction is exactly the direction of spacing $d_s$. As shown in Fig. 7, xp indicates the distance from leading edge (LE) to the pivot, and the dimensionless pivot locations $x_p/c$. Three cases with lower, medium and upper pivots under $\lambda = 1$ are presented for convenient comparison with $x^{'}$ direction where $x_p/c$=0, 0.5 and 1.

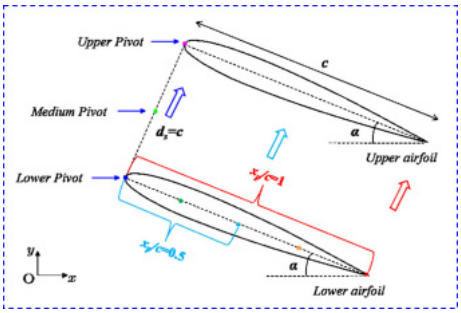


**Fig. 7** Schematic of pivot location change in $y^{'}$ direction for biplane airfoils under $\lambda = 1$.

Firstly, left subfigure of Fig. 8(a) tells us that four peak amplitudes decrease in turn and fluctuating curve of the lower airfoil equidistantly shifts backward as the pivot location rises in the $y^{'}$ direction. Most interestingly, the first peak swells to occupy more angles of attack and thus CL effectively increases with increasing $x_p/c$ during FTT. Similarly, left subfigure of Fig. 8(b) shows an absolutely different fluctuating trend with an outstanding second peak whereas next two peaks are flat gently for the upper airfoil. Secondly, stall angles of attack of the lower airfoil in STT are basically coincident even though the pivot in the $y^{'}$ direction locates on higher position as right subfigure of Fig. 8(a) and right subfigure of Fig. 8(b) show. But as pivot in the $x^{'}$ direction moves back, stall angle of attack will gradually increase. Due to $\alpha_{max} = 25°$, post-stall phase is shortened, implying the falling slope becomes greater. All in all, pivot locations should be arranged on the lower position closer to the trailing edge (TE).

The comparisons of moment coefficient ($C_M$) of biplane airfoils under various pivot location conditions are shown in Fig. 9. Here and below, the symbols $\downarrow$ and $\uparrow\uparrow$ are used to represent FTT and STT, respectively. At first glance, the pivots in the $y^{'}$ direction have significant impact on instantaneous $C_M$ and exceed instead influences of pivot backward movement. Besides, re-coincidences of those curves are about $8° \downarrow$ for the lower airfoil but $5° \downarrow$ for the upper airfoil in left subfigures of Figs. 9(a) and 9(b). $C_M$ curves of the lower airfoil fluctuate more violently in FTT comparing to the upper airfoil. These remarkable differences are deemed to interfere flow field in the gap by the vortex growth and shedding, which will be described later in Section 3.3. During STT, corresponding $C_M$ shows a downward trend from $-5° \uparrow\uparrow$ to $25° \uparrow\uparrow$ when the pivot rises in each subfigure. However, bifurcation points of $C_M$ of both airfoils are about $4° \uparrow\uparrow$.

Through comprehensive evaluation of the distribution characteristics of lift and moment coefficients, we think that medium pivot between two chords would bring out the optimized results.

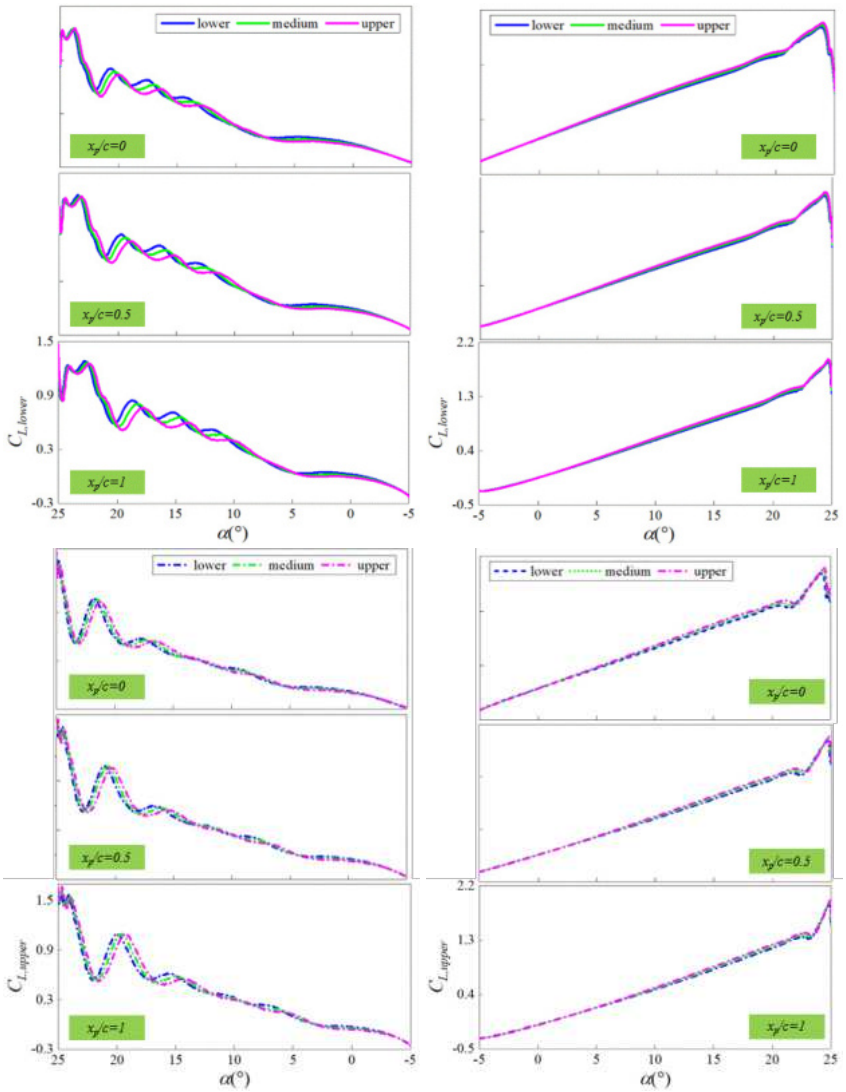


**Fig. 8** Lift coefficient change of (a) the lower airfoil in the first row, (b) the upper airfoil in the second row with $x_p/c = 0.25, 0.5, 1$ under $\lambda = 1$.

## 3.2 Effect of spacing

Under spacing ratio $\lambda$=0.25, 0.5 and 1, aerodynamic characteristics of tilting biplane airfoils are quite different as Fig. 10. In this section, medium pivot is selected, which locates in centerline between lower chord and upper chord, and $x_p/c$ is set to five levels: 0, 0.25, 0.5, 0.75 and 1.

Fig. 11 presents hysteresis of $C_{L,lower}$ and $C_{L,upper}$ for cases with various xp/c under $\lambda = 0.25$. Actually, if gap wall effect is strong enough, slender

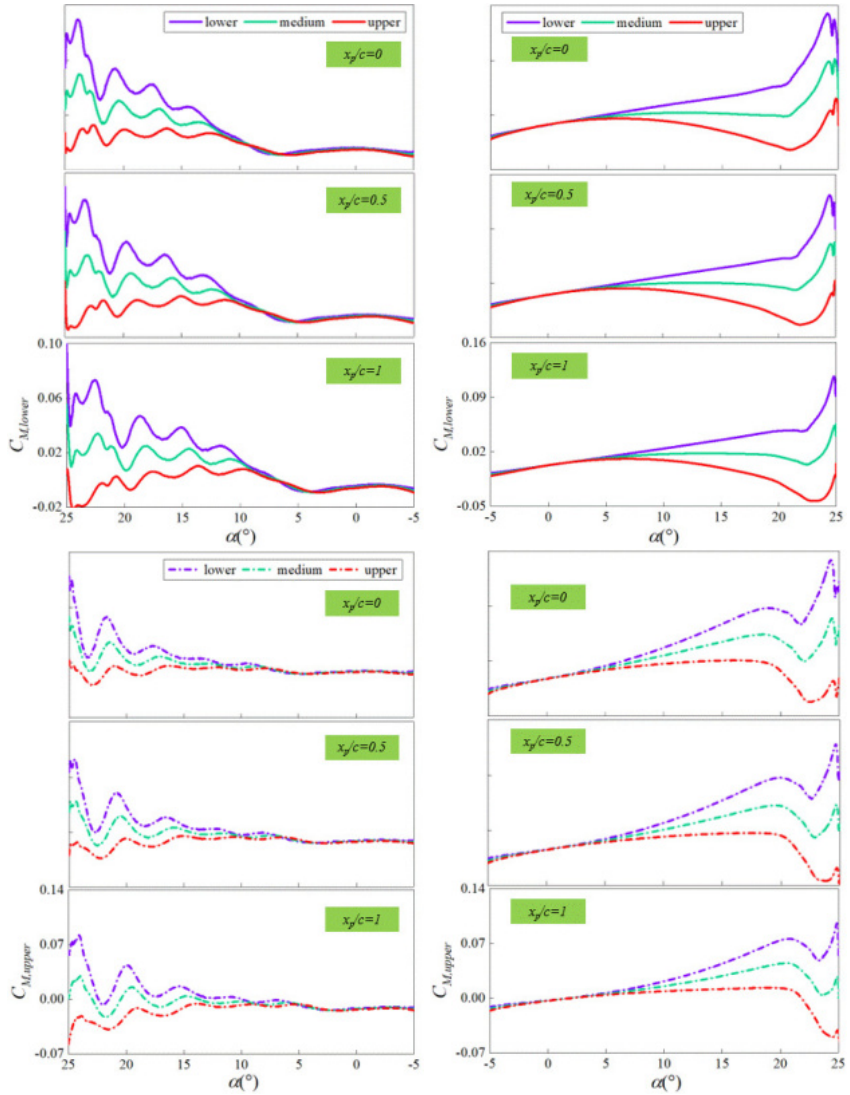


**Fig. 9** Moment coefficient change of (a) the lower airfoil in the first row, (b) the upper airfoil in the second row with $x_p/c = 0.25, 0.5, 1$ under $\lambda = 1$.

hysteresis will be upside down in Fig. 11(a), dictating $C_{L,lower} \downarrow$ almost are slightly greater than $C_{L,lower} \uparrow\uparrow$. But $C_{L,upper} \uparrow\uparrow$ obviously exceeds $C_{L,upper} \downarrow$ in Fig. 11(b). Although hysteresis shapes are distinct for two airfoils, the values of $C_{L,lower}$ are higher than $C_{L,upper}$ throughout the angle of attack. Additionally, it is clearly noticed that a regular phase lag with increasing $x_p/c$. During FTT,$C_{L,lower}$ and $C_{L,upper}$ behave with a violent fluctuation that originates in vortex shedding after dynamic stall, and the maximum exists under $x_p/c = 1$. At the same time, curves of $C_{L,lower} \downarrow$ and $C_{L,upper} \downarrow$ shift upwards

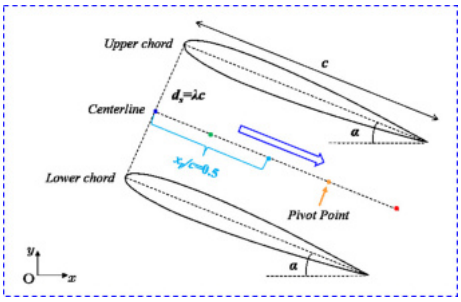


**Fig. 10** Schematic of pivot location change in $x^{'}$ direction for biplane airfoils.

as $x_p/c$ increases. On the contrary, the further the pivot is fixed from LE, the more negative force contribution generates in STT, and curves of $C_{L,lower}$ ↑↑ and $C_{L,upper}$ ↑↑ smoothly descent thus their maximum values appear under $x_p/c = 0$.

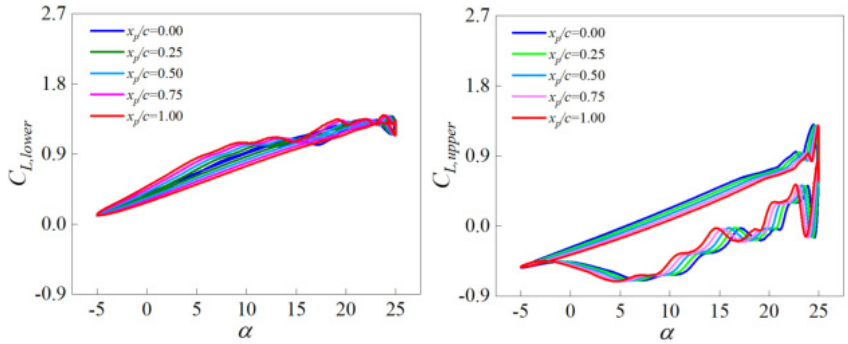


**Fig. 11** The relationships of lift coefficient and angle of attack for (a) the lower airfoil, (b) the upper airfoil for five fixed-pivot cases in λ=0.25.

Fig. 12 depicts the pressure contours for several typical angles of attack in a cycle under $x_p/c = 0$. In general, pressure around the lower airfoil distributes just as a single airfoil except for negative angle of attack, signifying that its pressure surface is a high-pressure region. However, the pressure surface of the upper airfoil behaves relative low pressure because the flow speeds up to pass through the gap. This is the reason why most $C_{L,upper}$ show negative values. Vortex shedding in FFT takes away a lot of energy and low pressure becomes more serious to effectively increase pressure difference though pressure section of the lower airfoil has larger high-pressure region, which directly leads to the reversal of $C_{L,lower}$ hysteresis. Besides, if there is not flow separation, it would be credible to regard pressure contours of two tilting transition modes as alike. Yet for higher angles of attack such as $\alpha = 10°$ and $\alpha = 17.5°$, boundary layer separation in FTT leads to wake vortices comparing to attachment in STT.

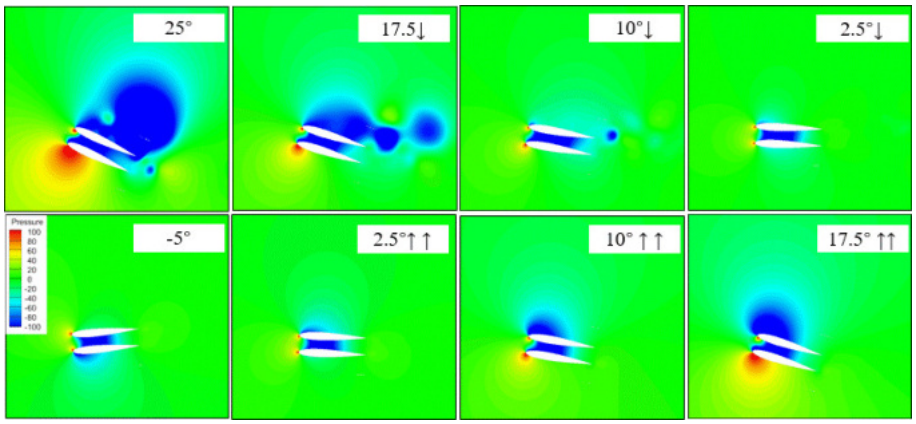


**Fig. 12** Contour plots of pressure fields around the pitching biplane airfoils in one cycle under $x_p/c$=0 and $\lambda$=0.25.

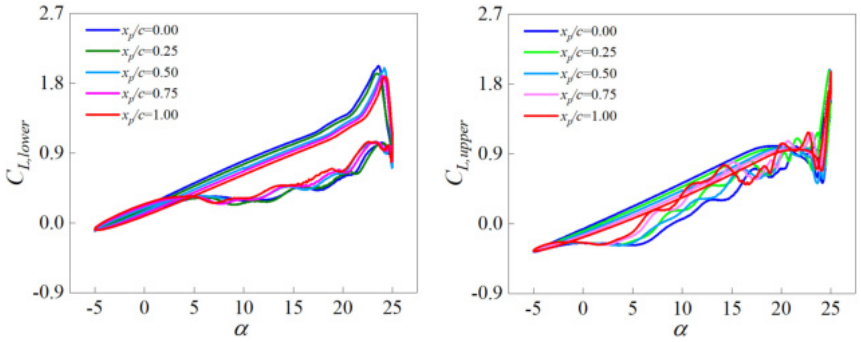


**Fig. 13** The relationships of lift coefficient and angle of attack for (a) the lower airfoil, (b) the upper airfoil for five fixed-pivot cases in $\lambda$=0.5.

Fig. 13 shows the hysteresis loops for cases with various xp/c under $\lambda$=0.5. Enlarged spacing weakens the wall effect in the gap, so hysteresis of $C_{L,lower}$ effectively swell. Meanwhile, fluctuating $C_{L,upper}$ ↓ sometimes are above smooth $C_{L,upper}$ ↑↑ especially for some peak parts. It can be explained by pressure distribution around biplane airfoils in Fig. 14. At $\alpha = 17.5°$ ↓, high-pressure region areas of the upper airfoil are nearly the equivalent of the lower airfoil in size, but it differs much at $\alpha = 17.5°$ ↑↑. Similarly, unsteady vortex shedding will occur in FTT to realize pressurization. The only thing worth pointing out is that the regularity of hysteresis shift under $\lambda$=0.5 is relatively chaotic, possibly due to gap vortex hindered growth, pending further exploration.

Fig. 15 shows that distributions of two groups of hysteresis have similar shapes and value ranges under $\lambda$=1, implying wall effect in the gap almost disappears. With the increase of $x_p/c$, hysteresis of $C_{L,lower}$ and $C_{L,upper}$ orderly collapse. Comparing to Figs. 12 and 14, contours in $\lambda$=1 are depicted in Fig. 16 need to be paid more attention to pressure distributions of two airfoils in each

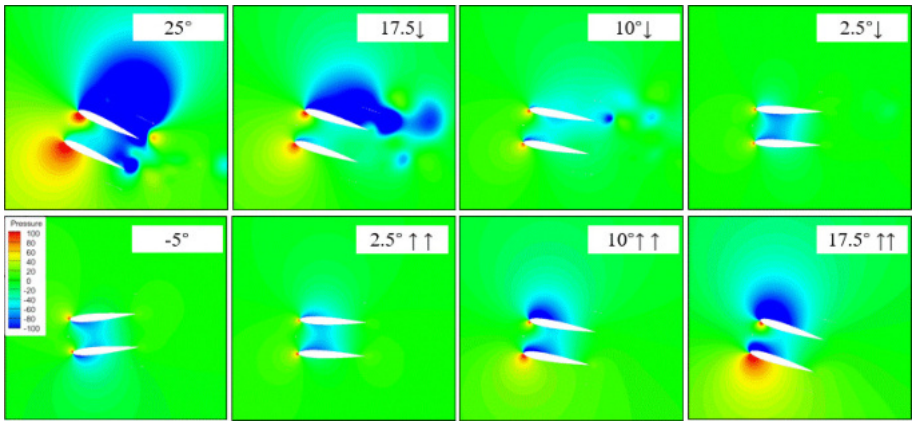


**Fig. 14** Contour plots of pressure fields around the pitching biplane airfoils in one cycle under $x_p/c$=0 and $\lambda$=0.5.

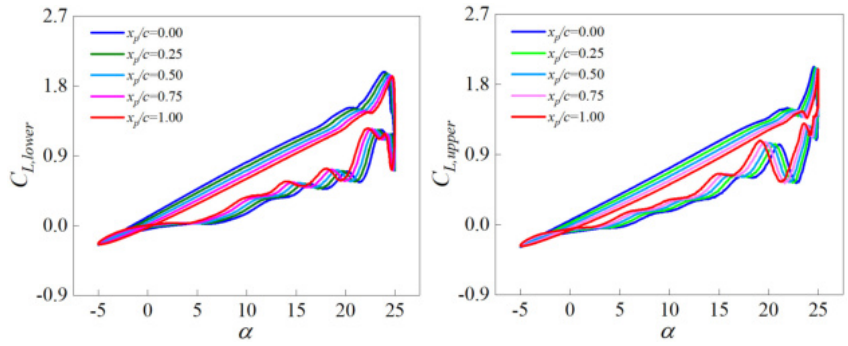


**Fig. 15** The relationships of lift coefficient and angle of attack for (a) the lower airfoil, (b) the upper airfoil for five fixed-pivot cases in $\lambda$=1.

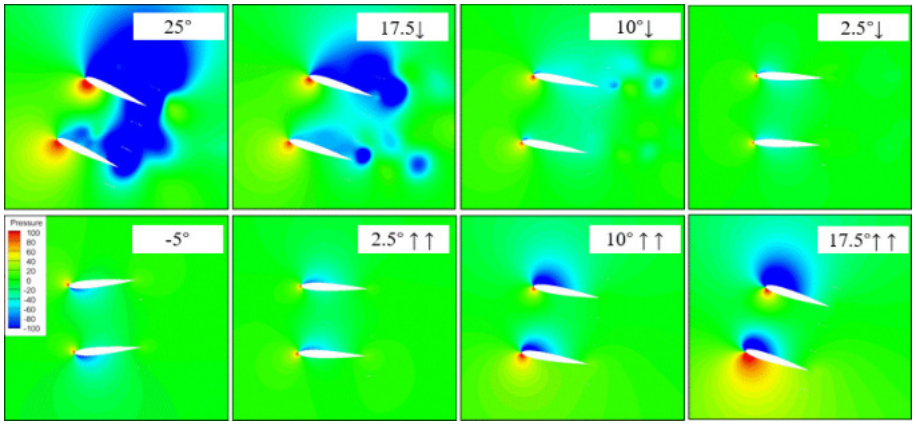


**Fig. 16** Contour plots of pressure fields around the pitching biplane airfoils in one cycle under $x_p/c$=0 and $\lambda$=1.

subfigure. Larger high-pressure region corresponds to smaller low-pressure region of suction surface resulting in resemble pressure difference. Yet the upper airfoil is still under greater influence induced by biplane configuration.

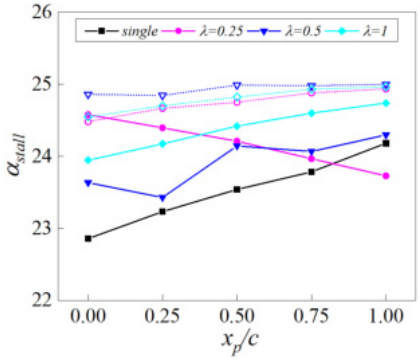


**Fig. 17** Variations of the stall angle of attack of biplane airfoils for five fixed pivots in different $\lambda$.

Fig. 17 reflects the variation in stall angle of attack $\alpha_{stall}$ with pivot locations, which also serves to illustrate some apparent effects of spacing on aerodynamic performances. The solid lines represent the lower airfoil, and dot lines indicates the upper airfoil, respectively. Interestingly, vast majority of biplane cases are higher than $\alpha_{stall}$ of a single airfoil along with an increasing trend. But due to extreme low pressure of the thin gap in $\lambda$=0.25, $\alpha_{stall}$ of the lower airfoil rapidly drags as pivot is closer to TE. Even though the wall effect is nearly diminished, rising $\alpha_{stall}$ of the lower airfoil still has difficulty in $\lambda$=0.5 until interference becomes quite weak under $\lambda$=1. No matter what spacing and pivot are arranged, $\alpha_{stall}$ slightly rises with further-back pivot location yet increases first then reduces with increasing $\lambda$.

Fig. 18 shows the total lift coefficient of biplane airfoils with a backward movement of the pivot point in comparison to a single airfoil. The overall curve appearances have no significant changes respective to the single one while the biplane airfoil $C_{L,total}$ varies in a larger range and their inclinations are steeper. Generally, the pivot location fixed in the TE point during FTT brings about better aerodynamic respond as $\alpha$ increases. However, the pivot locating on the LE point has greater $C_{L,total}$ within STT of biplane airfoils. Besides, phase lag almost doubles a single airfoil.

### 3.3 Vortical structures around biplane airfoils

Figs. 19 20 exhibit the vortical structures of different cases at the same angle of attack ($\alpha = 23.5°$), whose abundant flow structures can be observed clearly. Medium pivots are still be adopted in this subsection. Even if at the same angle of attack, the flow structures exist significant differences between FTT and

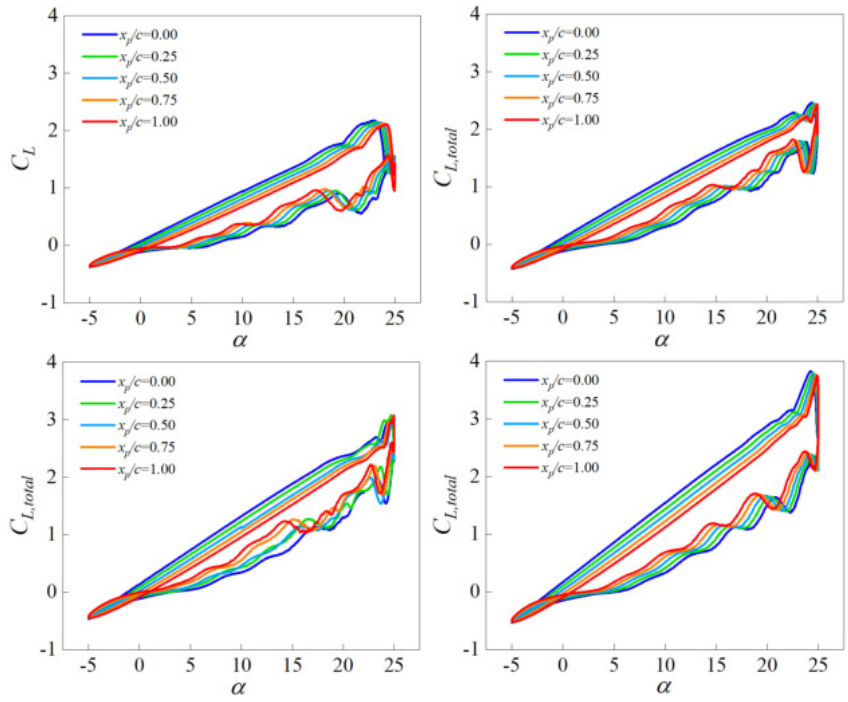


**Fig. 18** Total aerodynamic results for five fixed-pivot cases of (a) a single airfoil and biplane airfoils under (b) $\lambda$=0.25, (c) $\lambda$=0.5, (d) $\lambda$=1.

STT. For $\alpha = 23.5° \downarrow$, leading-edge vortex (LEV) and trailing-edge vortex (TEV) shed alternately to form wake and form the perspective of wake vortices, they are closer to biplane airfoils from $x_p/c = 0$ to $x_p/c = 1$, implying backer pivot induces vorticity evolution delay. Intuitively, LEVs with larger scale develop under larger $\lambda$ so that better aerodynamics could be provided. Moreover, the pivot point fixed on TE helps LEV attached on suction surfaces to last more time and thus improve $C_{L,total}$. However, turbulence changes more intense because of the inertia of the flow field.

And the converse is equally true: firstly for $\alpha = 23.5° \uparrow\uparrow$, secondary vortex (SV) generates to make LEV shed to the wake and its evolution is impacted by the pivot point location, from each line, we can be aware that the closer to LE, the more evident SV is, indicating the pivot point fixed on LE leads to higher $C_{L,total}$ in STT. Secondly, LEV of the lower airfoil is compressed by the upper airfoil when $\lambda$ decreases. It means that LEV covers the suction surface of the lower airfoil fully to improve aerodynamic loads. Thirdly, vortical evolution of the upper airfoil delays because of relative rear position. Their formations are rarely affected by the other airfoil and always parallel with the single one.

The above analysis about vorticity evolutions is completely consistent with the change of hysteresis of $C_L$, and it is more worth pondering to angle of attack and pivot point location have homologous flow structures such as LEV,

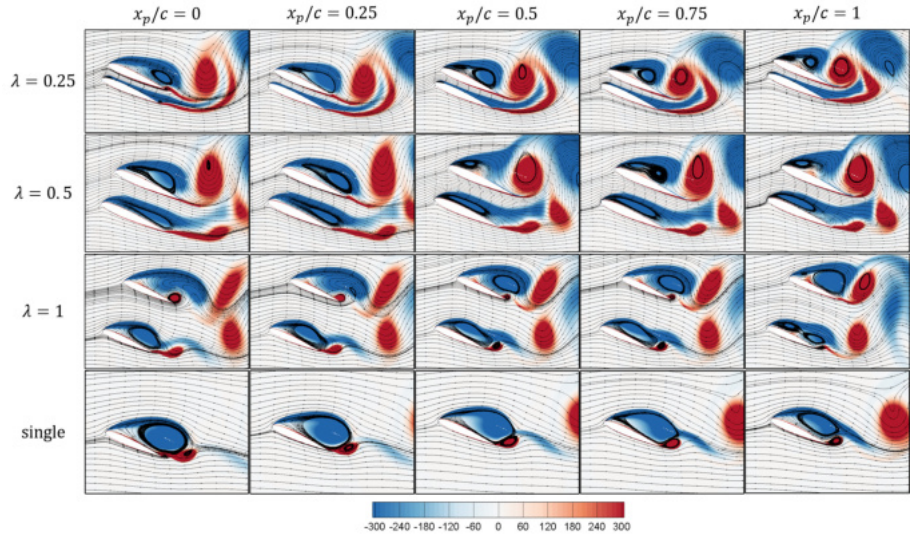


**Fig. 19** Vortical structure under different $x_p$ and $\lambda$ at 23.5° ↓.

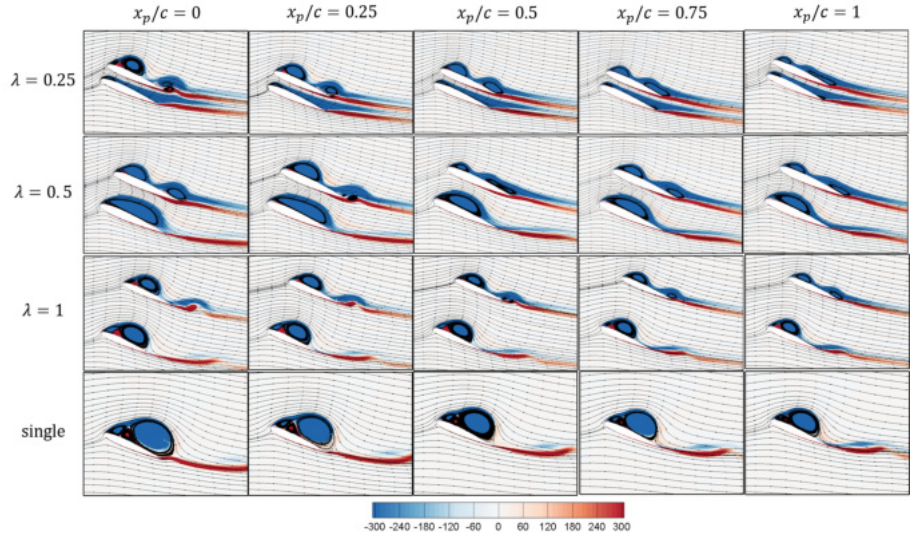


**Fig. 20** Vortical structure under different $x_p$ and $\lambda$ at 23.5° ↑↑.

TEV and SV. Therefore, effect of pivot could be explained by the concept of effective angle of attack.

### 3.4 Effective angle of attack of biplane airfoils

Logically, changing the pivot location is equivalent to adding additional translational motion if the reduced frequency is small enough [32]. When the pivot point is not on the chord line, the original motion is supposed to add a certain extent "plunging" due to the spacing effect. Therefore, it is suitable for the concept of the effective angle of attack $\alpha_{eff}$ to concern the additional velocity caused by the "plunging" motion. Generally, $\alpha_{geo} \geq 0°$ roughly simulates tilting transition of the biplane aircraft.

In Fig. 21, for the tilting airfoils whose pivot point is fixed on the centerline between biplane chords, the spacing ratio $\lambda$ will become one of the dominant factors. Assume that the midpoint of the line between two LE points is arranged as the coordinate origin, the length from the pivot point to the origin is $s_0$ and geometric angle of attack $\alpha_{geo}(t) = \alpha(t)$. First of all, in $x^{'}Oy^{'}$ coordinate system, different pivot corresponds to different speeds $v_p = \omega \cdot L = 2\pi f \cdot L$. Here, $L$ is the distance from each point $P_{u(l)}$ on the chord to the pivot point.

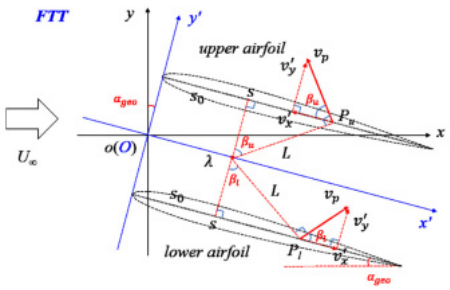


**Fig. 21** Schematic of the global coordinate system, parameter definition for FTT of biplane airfoils.

$$L = \sqrt{\left(\frac{\lambda c}{2}\right)^2 + (s - s_0)^2} \tag{4}$$

where $s$ represents the distance from the infinitesimal point $P$ to the LE point along the chord.

Taking the upper airfoil as an example, its local position angle due to pivot set-up $\beta_u$ is denoted as Eq. (5).

$$\beta_u(s, \lambda) = \arctan\left(\frac{2|s - s_0|}{\lambda c}\right) \tag{5}$$

Decompose $v_p$ in $x^{'}$ and $y^{'}$ directions:

$$v_x^{'}(s, \lambda) = v_p \cdot \cos(\beta_u) \tag{6}$$

$$v_y^{'}(s,\lambda) = v_p \cdot \sin(\beta_u) \tag{7}$$

Next, we convert from the coordinate system $x^{'}Oy^{'}$ to the coordinate system $xoy$, the transformation relationship of velocity components during FTT is as follows:

$$\begin{bmatrix} v_x \\ v_y \end{bmatrix} = \begin{bmatrix} \cos(\alpha_{geo}) & \sin(\alpha_{geo}) \\ -\sin(\alpha_{geo}) & \cos(\alpha_{geo}) \end{bmatrix} = \begin{bmatrix} v_p \cdot \cos(\alpha_{geo} - \beta_u) \\ v_p \cdot \sin(\alpha_{geo} - \beta_u) \end{bmatrix} \tag{8}$$

If considering $\lambda$, the additional angle of attack for the upper airfoil is calculated as the below form:

$$\alpha^*_{eff-u}(s,\lambda,t) = \arctan\left[\frac{v_y(s,\lambda,t)}{v_x(s,\lambda,t) + U_\infty}\right] \tag{9}$$

Just like the upper airfoil, the same transformation relationship is described for the lower airfoil in Eq. (10).

$$\begin{bmatrix} v_x \\ v_y \end{bmatrix} = \begin{bmatrix} \cos(\alpha_{geo}) & \sin(\alpha_{geo}) \\ -\sin(\alpha_{geo}) & \cos(\alpha_{geo}) \end{bmatrix} = \begin{bmatrix} v_p \cdot \cos(\alpha_{geo} - \beta_l) \\ v_p \cdot \sin(\alpha_{geo} - \beta_l) \end{bmatrix} \tag{10}$$

Here, $\beta_l = \beta_u$. Otherwise, the additional angle of attack for the lower airfoil $\alpha^*_{eff-l}$ remains unalterable.

$$\alpha^*_{eff-l}(s,\lambda,t) = \arctan\left[\frac{v_y(s,\lambda,t)}{v_x(s,\lambda,t) + U_\infty}\right] \tag{11}$$

Eventually, we take an infinitesimal length to derive the overall-averaged effective angle of attack by integrating in Eq. (12). In the below mathematical expression, $\alpha^*_{eff-l}$ includes a new factor $\lambda$ to represent the spacing effect of the biplane airfoils.

Furthermore, we note that transformation relationships of STT of biplane airfoils (Fig. 22) are exactly the same as FTT. It is easy to obverse that $\alpha_{eff}(\lambda,t)$ is highly nonlinear and time-varying.

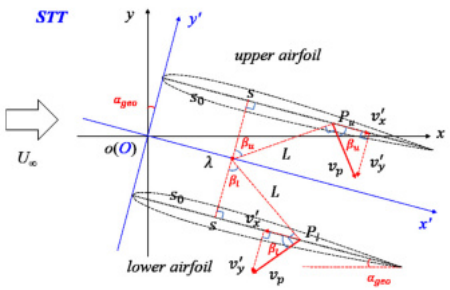


**Fig. 22** Schematic of the global coordinate system, parameter definition for STT of biplane airfoils.

For different pivot locations $x_p/c$=0, 0.25, 0.5, 0.75 and 1, their results are scaling about the medium points ($x_p/c = 0.5$) considering the local position angles $\beta_u$ and $\beta_l$. Fig. 23 is the data assimilation results based on $\alpha_{eff}$ redefined in Eq. (12). An interesting finding is that all curves become perfectly uniform except for slight deviation in FTT under $\lambda$=0.5 in Fig. 23(b). There are two speculations: one is calculation error, the other is vortex adhesion. It reveals the flow physics for the influence of the pivot point on the aerodynamic characteristics of tilting biplane airfoils, thus the effective angle of attack $\alpha_{eff}$ is a dominant factor.

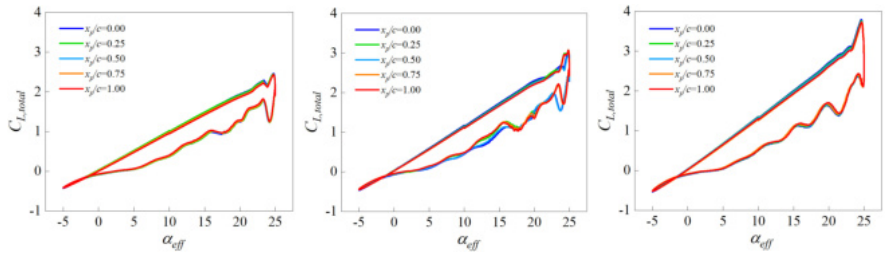


**Fig. 23** Data assimilation of total lift coefficient by the effective angle of attack for biplane airfoils under (a) $\lambda$=0.25, (b) $\lambda$=0.5, (c) $\lambda$=1.

Or look at it in this way: equivalent $C_{L,total}$ appears at the higher angle of attack when the pivot point moves from LE to TE. In fact, they are at the same effective angle of attack. At the unique $\alpha_{max} = 25°$, all kinds of flow structures are most visible, in this case, Fig. 24 exhibit the high sensitivity of vortical structure details for different pivot location xp. The first generation of LEVs are shedding due to the development of SV, simultaneously, the second LEVs are forming. While $\lambda$ is small, SV of the lower airfoil is inapparent but it does exist. In one cycle, SV destroys the original vorticity structures resulting in dynamic stall, yet stall for biplane airfoils is unviolent and delayed with respective to a single airfoil. In a word, biplane configuration provides higher aerodynamic loads and stability.

## 4 Conclusions

In this paper, computational investigation on aerodynamic characteristics of biplane airfoils was carried out to predict the tilting motion at high angle of attack. Two airfoils underwent sinusoidal pitching when the pivot point located in five different cases ($x_p/c$=0, 0.25, 0.5, 0.75, and 1) with three spacing ratios $\lambda$=0.25, 0.5 and 1. And downstroke corresponded to first tilting transition (FTT) and upstroke represented second tilting transition (STT). Pivot locations for three cases: lower pivot, medium pivot, and upper pivot, respectively, basically have highly similar effects on $C_L$, yet $C_M$ curves gradually descend along with upward movement of pivot points.

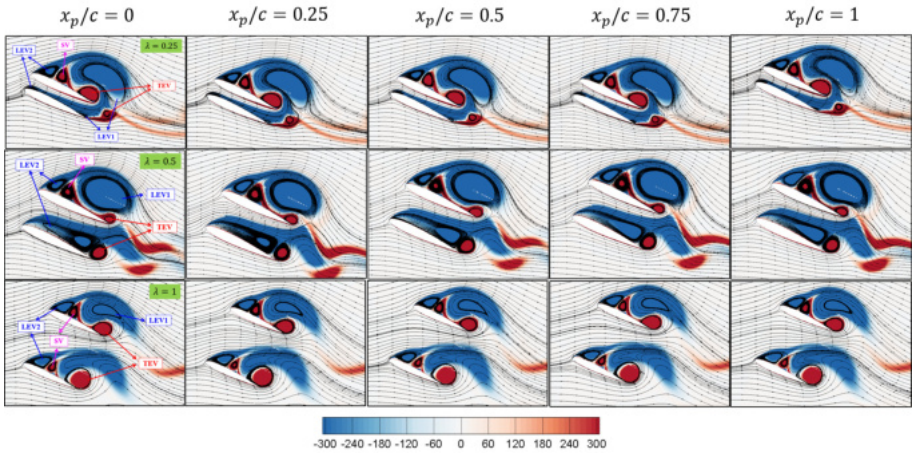


**Fig. 24** High similarity of vortical structure under different pivot locations and spacing ratios at angle of attack 25°.

But phase lag existed if the pivot location was arranged from LE to TE. It was the most notable that spacing effect had significant impact on $C_L$. Smooth part equidistantly drops but fluctuating part rises by the same way as $x_p/c$ increases. Hence, the best $C_L$ exists under $x_p/c = 0$ for STT and $x_p/c = 1$ for FTT. In general, hysteresis loops of biplane airfoils remain similar appearances with a single airfoil despite their area and inclination gradually swelled as $\lambda$ increased.

Moreover, vorticity structure presented that the flow evolution including LEV, SV and TEV had highly sensitivity to the pivot points. During FTT, the pivot point located on TE presented greater $C_L$. However, fixed pivot on LE could improve the aerodynamic responds in STT. Besides, relative higher $\lambda$ contributed to better aerodynamics of biplane airfoils and delayed its dynamic stall.

Last but not least, an integral form of the effective angle of attack $\alpha_{eff}$ for the biplane airfoils was proposed taking consideration of titling motion ($\alpha_{geo} \geq 0°$) and it were highly nonlinear and time-varying. The data assimilation results based on $\alpha_{eff}$ showed perfectly uniform after ignoring slight deviation. And vorticity structure details at the same $\alpha_{eff}$ distribute identically.

## Fundings

This paper was partially supported by the Innovation Guidance Fund Project of Innovation Academy for Light-duty Gas Turbine, CAS (Project CXYJJ20-ZD-03), Science and Technology Development Plan Project of Jilin Province (No. 20200201294JC), National Natural Science Foundation of China (grant number 11372309, 61304017), Provincial and Academic Cooperation Science

and Technology Special Fund (grant number 2020SYHZ0031), Chinese Academy of Sciences Youth Promotion Program (Project 2014192) and Chines Academy of Sciences Regional Development Young Scholars Program.

## Conflict of interest

The authors declare that they have no competing interests as defined by Springer, or other interests that might be perceived to influence the results and/or discussion reported in this paper.

## Ethical approval

This paper does not involve entrical issues for there are no animal or human experiments designed.

## Informed consent

There is no clinical trial in this paper, so patients' informed consent is not required.

## Author contribution

Ruixue Guo: Methodology, Validation, Formal analysis, Investigation, Writing-Original Draft, Visualization, Revision.

Xinbiao Pei: Writing- Reviewing and Editing, Funding acquisition.

Zheng Qiao: Writing-Reviewing and Editing, Project administration.

Yue Bai: Conceptualization, Resources, Writing- Reviewing and Editing, Supervision, Funding acquisition.

## References

1. Amiralaei, M. R., Alighanbari, H., & Hashemi, S. M.: An investigation into the effects of unsteady parameters on the aerodynamics of a low Reynolds number pitching airfoil. Journal of Fluids and Structures, 26(6), 979-993 (2010)
2. Lu, K., Xie, Y. H., & Zhang, D.: Numerical study of large amplitude, nonsinusoidal motion and camber effects on pitching airfoil propulsion. Journal of Fluids and Structures, 36(11), 184-194 (2013)
3. Rahromostaqim, M., Posa, A., & Balaras, E.: Numerical Investigation of the Performance of Pitching Airfoils at High Amplitudes. AIAA Journal, 53(8), 1-12 (2016)
4. Kim, D. H., & Chang, J. W. Low-Reynolds-number effect on the aerodynammic characteristics of a pitching NACA0012 airfoil. Aerospace Science and Technology. (2013)
5. Buchner, A. J., & Soria, J.: Measurements of the flow due to a rapidly pitching plate using time resolved high resolution PIV. Aerospace Science and Technology, 44(jul.-aug.), 4-17 (2014)

6. Wang, S., Zhou, Y., Alam, M. M., & Yang, H.: Turbulent intensity and Reynolds number effects on an airfoil at low Reynolds numbers. Physics of Fluids, 26(11), 257-263 (2014)
7. Guo, H., Hu, J., Guo, C. Y., Zhang, W. P., & Lin, J. F.: Numerical simulation of the dynamic stall of a freely rotating hydrofoil. Physics of Fluids, 32, 095113 (2020)
8. Zhou, T., Dowell, E., & Feng, S. S.: Computational investigation of wind tunnel wall effects on buffeting flow and lock-in for an airfoil at high angle of attack. Aerospace Science and Technology, 95, 105492- (2019)
9. Zhu, B., Zhang, J., & Zhang, W.: Impact of the ground effect on the energy extraction properties of a flapping wing. Ocean Engineering, 209, 107376 (2020)
10. Wu, J., Shu, C., Zhao, N., & Tian, F. B.: Numerical study on the power extraction performance of a flapping foil with a flexible tail. Physics of Fluids, 27(1), 277-292 (2015)
11. Mackowski, A. W., & Williamson, C. H. K.: Direct measurement of thrust and efficiency of an airfoil undergoing pure pitching. Journal of Fluid Mechanics, 765, 524-543 (2015)
12. Goyaniuk, L., Poirel, D., & Benaissa, A.: Pitch–heave symmetric stall flutter of a naca0012 at transitional Reynolds numbers. AIAA Journal, 1-12 (2020)
13. Liu, J., & Xiao, Z. X.: Low-frequency oscillation over naca0015 airfoil near stall at high Reynolds number. AIAA Journal, 58(1), 1-8 (2019)
14. Eljack, E. M., & Soria, J.: Investigation of the low-frequency oscillations in the flowfield about an airfoil. AIAA Journal. (2020)
15. Zhu, Y. H., Su, Y. X. , & Breuer, K.: Nonlinear flow-induced instability of an elastically mounted pitching wing. Journal of Fluid Mechanics, 899, A35 (2020)
16. Tay, W. B., Bijl, H., & Oudheusden, B.: Biplane and tail effects in flapping flight. AIAA Journal, 51(9), 2133-2146 (2013)
17. Faure, T. M., Dumas, L., & Montagnier, O.: Numerical study of two-airfoil arrangements by a discrete vortex method. Theoretical and Computational Fluid Dynamics, 34(2) (2020)
18. Jones, R., Cleaver, D. J., & Gursul, I.: Aerodynamics of biplane and tandem wings at low Reynolds numbers. Experiments in Fluids, 56:124 (2015)
19. Lagopoulos, N. S., Weymouth, G. D., & Ganapathisubramani, B.: Deflected wake interaction of tandem flapping foils. Journal of Fluid Mechanics, 903, A3 (2020)
20. Alcántara, A. M, Feria, R. F., & Rojas, E. S.: Vortex flow structures and interactions for the optimum thrust efficiency of a heaving airfoil at different mean angles of attack. Physics of Fluids, 27(7), 329-350 (2015)
21. Baik, Y. S., Bernal, L. P., Granlund, K., & Ol, M. V.: Unsteady force generation and vortex dynamics of pitching and plunging airfoils. Journal of Fluid Mechanics, 709, 37-68 (2012)
22. Miao, J. M., Surf, W. H., & Tai, C. H.: Numerical analysis on aerodynamic force generation of biplane counter-flapping flexible airfoils. Journal of Aircraft, 46(5), 1785-1794 (2009)
23. Cong, L. F., Teng, B., & Cheng, L.: Hydrodynamic behavior of two-dimensional tandem-arranged flapping flexible foils in uniform flow. Physics of Fluids, 32(2), 021903 (2020)
24. Kaya, M., Tuncer, I. H., Jones, K. D., & Platzer, M. F.: Optimization of flapping motion parameters for two airfoils in a biplane configuration. Journal of Aircraft, 46(2), 583-592 (2015)
25. Lua, K. B., Lu, H., Zhang, X. H., Lim, T. T., & Yeo, K. S.: Aerodynamics of two-dimensional flapping wings in tandem configuration. Physics of Fluids, 28(12), 121901 (2016)
26. Zhu, J. Y., & Lei, B.: Effect of wing-wing interaction on the propulsive performance of two flapping wings at biplane configuration. Applied Bionics and Biomechanics, 2018, 1-12 (2018)
27. Zhu, J. Y., & Zhang, J. C.: Power extraction performance of two semi-active flapping airfoils at biplane configuration. Journal of Mechanical Science and Technology, 34(1), 175-187 (2020)
28. Zhou, H., Wang, G., & Liu, Z. K.: Numerical analysis on flutter of Busemann-type supersonic biplane airfoil. Journal of Fluids and Structures, 92, 102788 (2020)
29. Granlund, K. O., Ol, M. V., & Bernal, L. P.: Unsteady pitching flat plates. Journal of Fluid Mechanics, 733, R5 (2013)
30. Mackowski, A. W., & Williamson, C. H. K.: Effect of pivot location and passive heave on propulsion from a pitching airfoil. Physical Review Fluids, 2, 013101 (2017)

31. Yu, Y. L., Amandolese, X., Fan, C. W., & Liu, Y. Z.: Experimental study and modelling of unsteady aerodynamic forces and moment on flat plate in high amplitude pitch ramp motion. Journal of Fluid Mechanics, 846, 82-120 (2018)
32. Li, X., Feng, L. H., & Li, Z. Y.: Flow mechanism for the effect of pivot point on the aerodynamic characteristics of a pitching airfoil and its manipulation. Physics of Fluids, 31(8), 087108 (2019)
33. Yu, H. T., & Bernal, L. P.: Effects of pivot location and reduced pitch rate on pitching rectangular flat plates. AIAA Journal, 55(3), 1-17 (2016)
34. Tian, W., Bodling, A., Liu, H., Wu, J. C., He, G. W., & Hu, H.: An experimental study of the effects of pitch-pivot-point location on the propulsion performance of a pitching airfoil. Journal of Fluids and Structures, 60, 130-142 (2016)
35. Wang, S. Y, Ingham, D. B., Ma, L., Pourkashanian, M., & Zhi, T.: Turbulence modeling of deep dynamic stall at relatively low Reynolds number. Journal of Fluids and Structures, 33, 191-209 (2012)
36. Wang, S. Y., Ingham, D. B., Ma, L., Pourkashanian, M., & Zhi, T.: Numerical investigations on dynamic stall of low Reynolds number flow around oscillating airfoils. Computers & Fluids, 39(9), 1529-1541 (2010)
37. Karbasian, H. R., & Kim, K. C.: Numerical investigations on flow structure and behavior of vortices in the dynamic stall of an oscillating pitching hydrofoil. Ocean Engineering, 127, 200-211 (2016)
38. Rahman, A., & Tafti, D.: The role of vortex–vortex interactions in thrust production for a plunging flat plate. Journal of Fluids and Structures, 96, 103011 (2020)
39. Zhou, T., Zhong, S. Y., & Fang, Y.: Trailing-edge boundary layer characteristics of a pitching airfoil at a low Reynolds number. Physics of Fluids, 33(3), 033605 (2021)
40. Almutairi, J., Ellack, E., & Alqadi, I.: Dynamics of laminar separation bubble over naca-0012 airfoil near stall conditions. Aerospace Science and Technology, 68(sep.), 193-203 (2017)
41. Zhang, X. Y., Kheiri, M., & Xie, W. F.: Nonlinear dynamics and gust response of a two-dimensional wing. International Journal of Non-Linear Mechanics, 123, 103478 (2020)
42. Kuya, Y., Boda, K., & Sawada, K.: Numerical study of transonic shock buffet control over a supercritical airfoil. Journal of Aircraft, 46(5), 1785-1794 (2020)
43. Lee, T., & Gerontakos, P. Investigation of flow over an oscillating airfoil. Journal of Fluid Mechanics, 512, 313–341 (2004)
44. Gharali, K. & Johnson, D. A.: Dynamic stall simulation of a pitching airfoil under unsteady freestream velocity. Journal of Fluids and Structures, 42, 228–244 (2013)